

NEW NEARBY HYPERVELOCITY STARS AND THEIR SPATIAL DISTRIBUTION FROM GAIA DR2

CUIHUA DU¹, HEFAN LI², YEPENG YAN², HEIDI JO NEWBERG³, JIANRONG SHI^{4,1}, JUN MA^{4,1}, YUQIN CHEN^{4,1}, ZHENYU WU^{4,1}

¹College of Astronomy and Space Sciences, University of Chinese Academy of Sciences, Beijing 100049, China; ducuihua@ucas.ac.cn

²School of Physical Sciences, University of Chinese Academy of Sciences, Beijing 100049, China

³Department of Physics, Applied Physics and Astronomy, Rensselaer Polytechnic Institute, Troy, NY 12180, USA

⁴Key Laboratory of Optical Astronomy, National Astronomical Observatories, Chinese Academy of Sciences, Beijing 100012, China

Draft version July 16, 2019

ABSTRACT

Base on about 4,500 large tangential velocity ($V_{\text{tan}} > 0.75V_{\text{esc}}$) with high-precision proper motions and 5σ parallaxes in Gaia DR2 5D information derived from parallax and proper motion, we identify more than 600 high velocity stars with 50% unbound probability. Of these, 28 nearby (less than 6 kpc) late-type Hypervelocity stars (HVSs) with over 99% possibility of unbound are discovered. In order to search for the unbound stars from the full Gaia DR2 6D phase space information derived from parallax, proper motion and radial velocity, we also identify 28 stars from the total velocity ($V_{\text{gc}} > 0.75V_{\text{esc}}$) that have probabilities greater than 50% of being unbound from the Galaxy. Of these, only three have a nearly 99% probabilities of being unbound. On the whole HVSs subsample, there is 12 sources reported by other surveys. We study the spatial distribution of angular positions and angular separation of HVSs. We find the unbound HVSs are spatially anisotropic that is most significant in the Galactic longitude at more than 3σ level, and lower unbound probability HVSs are systematically more isotropic. The spatial distribution can reflect the origin of HVSs and we discuss the possible origin link with the anisotropy.

Subject headings: Galaxy:center-Galaxy:kinematics and dynamics-Galaxy:stellar content

1. INTRODUCTION

Hypervelocity stars (HVSs) are unbound stars escaping the gravitational potential of the Galaxy. Hills (1988) predicted their existence as an interaction consequence of a binary star system and the massive black hole (MBH) in the Galactic Center (GC). In 2005, Brown et al. (2005) discovered a late B-type main-sequence star having heliocentric radial velocity of $853 \pm 12 \text{ km s}^{-1}$, which is significantly in excess of the Galactic escape speed at that location. Following the discovery of the first HVS by Brown et al. (2005), a large number of HVSs candidates have been reported (e.g., Hirsch et al. 2005; Edelmann et al. 2005; Brown et al. 2006, 2009, 2012, 2014; Li et al. 2012, 2018; Zheng et al. 2014; Geier et al. 2015; Huang et al. 2017; Du et al. 2018b; Marchetti et al. 2018; Bromley et al. 2018; Hattori et al. 2018; Boubert et al. 2018; Shen et al. 2018). HVSs can not only probe the extreme dynamics and physical processes at the GC, but also can be used as dynamical tracers of integral properties of the Galaxy. Such stars can be used to probe the star formation in the GC or constrain the potential of the Milky Way (e.g. Gnedin et al. 2005), some studies have used the kinematics of HVSs to obtain an estimate of the Galaxy mass (e.g. Smith et al. 2007; Piffl et al. 2014). There have been a few studies aimed at combining their chemical and kinematic information to get a picture of where these stars are produced and how they achieve such high velocities or to determine the origin of HVS (e.g. Bromley et al. 2009; Purcell et al. 2010; Wang et al. 2009, 2013; Hawkins et al. 2015; Geier et al. 2015; Tauris 2015; Ziegerer et al. 2017; Marchetti et al. 2018; Du et al. 2018a,b; Irrgang et al. 2018).

Before Gaia DR2 release, most of the confirmed HVSs are massive early-type O- and B-type stars in the Galactic halo due to the selections bias of target surveys. But the HVS is not restricted to early-type stars, but is also observed among evolved low-mass stars such as hot subdwarf stars (Hirsch et

al. 2005; Geier et al. 2015) and white dwarfs (Vennes et al. 2017; Raddi et al. 2018; Shen et al. 2018). Even some studies have been devoted to search for late-type HVSs candidates. For example, Kollmeier et al. (2009, 2010) attempted to find metal-rich, old-populations F/G type HVSs from Sloan Digital Sky Survey (SDSS) data. However, such late-type old-population HVSs have not been detected only places a upper limit on the rate of ejection. Li et al. (2012) reported the discovery of 13 F-type HVSs, located at distances ranging from 3 kpc to 10 kpc. Palladino et al. (2014) found 20 low-mass G- and K-type HVS candidates from SDSS by incorporating proper motions, but none of the orbits were consistent with GC ejection. However, Ziegerer et al. (2015) reanalyzed the proper motions for 14 of these and found that they are all bound to the Galaxy and the initial HVS classification was due to the flawed proper motions. Zhong et al. (2014) reported the discovery of 28 HVSs candidates which covered a broad color range at heliocentric distance of less than 3 kpc from Large Sky Area Multi-object Fiber Spectroscopic Telescope (LAMOST) DR1. Vickers et al. (2015) used more stringent proper motions cuts to carry out a study of the runaway population of low-mass star in SDSS, they detected a number of high-velocity runaway stars, but their HVSs candidates were marginal detections. Zhang et al. (2016) identified 29 metal-rich ($[\text{Fe}/\text{H}] > -0.8$) high velocity stars, but they did not find any candidates which have velocities in excess of the escape speed.

After Gaia DR2 release, it has already been used to search for new HVSs that can be unbound to the Galaxy. For example, Hattori et al. (2018) reported the discovery of 30 stars with extreme velocities ($> 480 \text{ km s}^{-1}$) in Gaia DR2, one of them is consistent with having been ejected from GC, and another has orbit that passed near the Large Magellanic Cloud. Marchetti et al. (2018) found 20 HVSs have probabilities greater than 80% of being unbound from the Galaxy in

the subset of stars with radial velocity measurements of Gaia DR2. Du et al. (2018b) found 24 late-type high velocity stars with stellar astrometric parameters and radial velocities from Gaia DR2 and LAMOST data. Most of the high velocity stars are metal-poor and α -enhanced. Of these, 6 stars belong to hypervelocity stars. Bromley et al. (2018) investigated the nature of nearby (10-15 kpc) high-speed stars in Gaia DR2 and identified two have 100% probability of unbound in over 100 high-speed stars. However, most previous surveys are based on the subsample of about 7 million stars with radial velocity measurements alone in Gaia DR2. As shown by Bromley et al. (2018), based on Gaia DR2 parallaxes and proper motions alone one can efficiently select relatively nearby high-speed candidates. Using the Galactic rest-frame tangential velocity should return a higher proportion of nearby HVSs than radial velocity (Kenyon et al. 2018). The tangential velocity need to use accurate proper motions and parallaxes with sufficiently small uncertainties.

In this study, our goal is to consider the wealth of accurate proper motions and parallaxes available in Gaia DR2 (Gaia Collaboration et al. 2018a,b) to obtain more HVSs and study the distribution of HVS angular position on the sky and judge if there is significantly anisotropic. The paper is structured as follows. In Section 2, we briefly describe the data and HVSs sample candidate selection. In Section 3, we show the observed spatial distribution of HVSs on the sky is anisotropic. In Section 4, we discuss the possible origin of spatial anisotropy of unbound HVSs. The conclusions and summary are given in Section 5.

2. DATA AND TARGET SELECTION

2.1. Gaia data

The Gaia satellite is a space-based mission launched in 2013 and started science operations the following year. The second Gaia data (Gaia DR2) includes high-precision measurements of nearly 1.7 billion stars (Gaia Collaboration et al. 2018a,b). As well as positions, the data include photometry, radial velocities, and information on astrophysical parameters and variability, for sources brighter than magnitude 21. The parallaxes, and mean proper motions for about 1.3 billion of the brightest stars are contained. Radial velocity measurements v_r for a subset of 7,224,631 stars are included in Gaia DR2 archive (Gaia Collaboration, et al. 2016) with an effective temperature from 3550 to 6990 K within a few thousand parsec of the Sun. The median uncertainty for the bright sources ($G < 14$ mag) is 0.04 mas, 0.1 mas at $G = 17$ mag, and 0.7 mas at $G = 20$ mag for the parallax, and 0.05, 0.2, and 1.2 mas yr^{-1} for the proper motions, respectively. More detailed description about the astrometric content of Gaia DR2 can be found in Lindegren et al. (2018).

In this study, we first select stars with parallax uncertainties smaller than 20%. In order to assure the quality of the reported radial velocity, we keep those sources that have $rv_nb_transits > 5$ in Gaia DR2 archive, indicating that v_r measurements were taken at a minimum of six distinct epochs. We do not adopt other cut on the astrometric solution. While a recent paper by Marchetti et al. (2018) adopted more conservative criteria for the quality of the Gaia astrometric solution. As mentioned by Hattori et al. (2018), the conservative cut on the quality of astrometric solution might potentially discard a lot of interesting candidate stars with small formal errors on parallax and proper motion. In addition, due to different Galactic potential model and different estimation

method about probability of being unbound, the HVSs sample could be different.

2.2. Distance derivation from Gaia parallaxes

According to the parallaxes and proper motions, distance and velocities could be inferred using those data. This is important task to derive distance and velocities, especially when parallaxes are involved because the effects of the observational errors on the parallaxes and the proper motions can lead to potentially strong biases (Luri et al. 2018). Butkevich et al. (2017) confirmed that due to various instrumental effects of Gaia satellite, in particular, to a certain kind of basic-angle variations, these can bias the parallax zero point of an astrometric solution derived from observations. From the quasars and validation solutions, Lindegren et al. (2018) estimated that systematics in the parallaxes depending on position, magnitude, and color are generally below 0.1 mas, but global parallax zero-point of Gaia observations is: $\varpi_{zp} = -0.029$ mas. Thus, it is necessary to subtract parallax zero-point (ϖ_{zp}) when parallax is used to calculate astrophysical quantities.

Despite the simple relation between the parallax and distance, inversion of the parallax to obtain distance is only appropriate when there are no measurement errors. While the significance of the parallax detections in the 5σ sample is high, parallax errors are not negligible. The parallax error distribution of Gaia DR2 sources is well approximated by a Gaussian with a tail extending to negative values (Lindegren et al. 2018). When deriving the distance by inverting the Gaia DR2 parallax, even small values allowed by the uncertainties may be unrealistic. By comparison of the heliocentric distance derived by inverting the Gaia DR2 parallax with derived by Bailer-Jones (2018) using a geometrical distance prior for our sample, we found that the distance derived by inverting the parallax is relative precise just for nearby (less than 2 kpc) sample stars. When the parallax error distribution is narrow compared to the measured parallax, the extending tail of the distribution are negligible especially for the nearby stars. So some studies selected only sources that have small relative parallax error (e.g. Hattori et al. 2018) to give a straightforward estimate of distance from the inverse of the parallax. A more general method, Bayesian approach, incorporates prior information about source location (Bailer-Jones 2015; Astraatmadja & Bailer-Jones 2016; Luri et al. 2018).

In this study, in order to derive relative accurate distance estimation for distant sample stars, we use the full Bayesian approach to infer distances (Luri et al. 2018). We use the exponentially decreasing space density prior in distance d with a most probable source location at $2L$ (Bailer-Jones 2018):

$$P(d | L) \propto d^2 \exp(-d/L)$$

Here, the length scale L depending on the sky location relative to the Galaxy (Bailer-Jones 2018) and we assume uniform priors on v_{ra}, v_{dec}, v_r . So we can express the posterior distribution:

$$P(\boldsymbol{\theta} | \mathbf{x}) \propto \exp[-\frac{1}{2}(\mathbf{x} - \mathbf{m}(\boldsymbol{\theta}))^T C_x^{-1}(\mathbf{x} - \mathbf{m}(\boldsymbol{\theta}))] P(d | L)$$

where $\boldsymbol{\theta} = (d, v_\alpha, v_\delta, v_r)^T$, $\mathbf{x} = (\varpi, \mu_\alpha^*, \mu_\delta, rv)^T$, $\mathbf{m} = (1/d, v_\alpha/kd, v_\delta/kd, v_r)^T$, $k = 4.74$ and C_x is covariance ma-

trix:

$$\begin{pmatrix} \sigma_{\varpi}^2 & \rho_{\varpi\alpha}^{\mu_{\alpha^*}} \sigma_{\varpi} \sigma_{\mu_{\alpha^*}} & \rho_{\varpi\delta}^{\mu_{\delta}} \sigma_{\varpi} \sigma_{\mu_{\delta}} & \rho_{\varpi rv}^{\mu_{\alpha^*}} \sigma_{\varpi} \sigma_{rv} \\ \rho_{\varpi\alpha}^{\mu_{\alpha^*}} \sigma_{\varpi} \sigma_{\mu_{\alpha^*}} & \sigma_{\mu_{\alpha^*}}^2 & \rho_{\mu_{\alpha^*}\delta}^{\mu_{\delta}} \sigma_{\mu_{\alpha^*}} \sigma_{\mu_{\delta}} & \rho_{\mu_{\alpha^*}rv}^{\mu_{\alpha^*}} \sigma_{\mu_{\alpha^*}} \sigma_{rv} \\ \rho_{\varpi\delta}^{\mu_{\delta}} \sigma_{\varpi} \sigma_{\mu_{\delta}} & \rho_{\mu_{\alpha^*}\delta}^{\mu_{\delta}} \sigma_{\mu_{\alpha^*}} \sigma_{\mu_{\delta}} & \sigma_{\mu_{\delta}}^2 & \rho_{\mu_{\delta}rv}^{\mu_{\delta}} \sigma_{\mu_{\delta}} \sigma_{rv} \\ \rho_{\varpi rv}^{\mu_{\alpha^*}} \sigma_{\varpi} \sigma_{rv} & \rho_{\mu_{\alpha^*}rv}^{\mu_{\alpha^*}} \sigma_{\mu_{\alpha^*}} \sigma_{rv} & \rho_{\mu_{\delta}rv}^{\mu_{\delta}} \sigma_{\mu_{\delta}} \sigma_{rv} & \sigma_{rv}^2 \end{pmatrix}$$

where ρ_i^j denotes the correlation coefficient between i and j , σ_k denotes the standard deviation of k and the correlation coefficient $\rho_i^{rv} = 0$, $i = \varpi, \mu_{\alpha^*}, \mu_{\delta}$.

2.3. Coordinate Systems and Velocity Computation

We then transform the Galactic coordinates (l, b) and heliocentric distance for the stars into a Cartesian Galactocentric coordinate system (X, Y, Z) , and derive the projected distance from the Galactic center using coordinate transformations (Bond et al. 2010):

$$\begin{aligned} X &= R_{\odot} - d \cos(b) \cos(l) \\ Y &= -d \cos(b) \sin(l) \\ Z &= d \sin(b) + z_{\odot} \end{aligned} \quad (1)$$

Here, we adopt the distance from the Sun to Galactic center $R_{\odot} = 8.2$ kpc (Bland-Hawthorn & Gerhard 2016), and the Sun has an offset from the local disk $z_{\odot} = 25$ pc (Jurić et al. 2008), d is distance from the star to the Sun, and (l, b) are the Galactic longitude and latitude. We adopt a Local Standard of Rest velocity $V_{\text{LSR}} = 232.8$ km s⁻¹ in the direction of rotation (McMillan 2017), and the solar peculiar motion $(V_X^{\odot, \text{pec}}, V_Y^{\odot, \text{pec}}, V_Z^{\odot, \text{pec}}) = (10.0$ km s⁻¹, 11.0 km s⁻¹, 7.0 km s⁻¹) (Tian et al. 2015; Bland-Hawthorn & Gerhard 2016). We calculate each star's Galactic space-velocity components from its tangential velocities, distance, and radial velocity (Johnson & Soderblom 1987).

$$\begin{aligned} V_X &= V_X^{\text{obs}} + V_X^{\odot, \text{pec}} \\ V_Y &= V_Y^{\text{obs}} + V_Y^{\odot, \text{pec}} + V_{\text{LSR}} \\ V_Z &= V_Z^{\text{obs}} + V_Z^{\odot, \text{pec}} \end{aligned} \quad (2)$$

We can use 6D phase space information to derive the total velocities V_{gc} in the Galactic rest frame and 5D information to derive the total tangential velocity V_{tan} . V_{tan} is the Galactic rest frame tangential velocity corrected for the solar motion, is given by:

$$\vec{V}_{\text{tan}} = \vec{v}_{\text{tan}} + \vec{V}^{\odot} - (\vec{V}^{\odot} \cdot \hat{r}) \hat{r} \quad (3)$$

where $\vec{v}_{\text{tan}} = (v_{\alpha}, v_{\delta})$, \vec{V}^{\odot} is the Sun's velocity in the Galaxy's rest frame, and \hat{r} is the unit vector in the direction of the Sun in that frame.

2.4. HVSS sample Candidate Selection

The escape speed V_{esc} at different Galactocentric distance can be derived by adopting a Galaxy potential model which is provided by McMillan (2017). Their model includes four components: the cold gas discs near the Galactic plane, the thin and thick stellar discs, a bulge and a dark-matter halo. The Galactic potential Φ is sum of potential of each component. We define unbound stars as ones which can reach the point with gravitational potential Φ_{max} and the local escape speed V_{esc} is given by:

$$V_{\text{esc}} = \sqrt{2[\Phi_{\text{max}} - \Phi(r_{\text{gc}})]} \quad (4)$$

where $\Phi(r)$ is the gravitational potential at r and r_{gc} is Galactocentric distance. We use the local escape speed 521 km s⁻¹ (Williams et al. 2017) to constrain the escape curve of McMillan (2017).

We first identified about 6,000 candidate stars with $V_{\text{tan}} > 0.75V_{\text{esc}}$ or $V_{\text{gc}} > 0.75V_{\text{esc}}$. For each star, we use Markov chain Monte Carlo (MCMC) sampler EMCEE (Goodman & Weare 2010; Foreman-Mackey et al. 2013) to estimate error of these stars. We run each chain using 20 walkers and 1000 steps (including 500 burn-in steps), for a total 10000 random samples drawn from the posterior distribution $P(\theta | x)$. We remove stars with $\sigma_V/V > 0.3$ and get 4565 candidate stars with $V_{\text{tan}} > 0.75V_{\text{esc}}$, 441 stars with $V_{\text{gc}} > 0.75V_{\text{esc}}$. For each star, we compute the probability P_{ub} of being unbound from the Galaxy as the fraction of Monte Carlo realization which result in an unbound orbit has $V_{\text{gc}} \geq V_{\text{esc}}$ at that given position.

Figure 1 shows the probability of unbound P_{ub} as a function of velocity in the Galactic rest-frame V_{gc} for stars with $V > 0.75V_{\text{esc}}$. The orange dots represent tangential velocity from 4565 candidates having proper motion in 5D information, and the blue dots represent the total velocity from 441 candidates having radial velocity and proper motion in 6D information. Next we identify HVSS that are potentially unbound to the Galaxy. There are 28 stars with the probability of unbound $P_{\text{ub}} > 0.99$ (red star) from 5D information and 28 stars with $P_{\text{ub}} > 0.5$ (red hexagon) from 6D information, which are shown in different signal of Figure 2.

In this figure, we give the velocity in the Galactic rest-frame V_{gc} as a function of Galactocentric distance r_{gc} for stars with $P_{\text{ub}} > 0.5$ (black dot) and with $P_{\text{ub}} > 0.99$ (red star) from 5D information and with $P_{\text{ub}} > 0.5$ (red hexagon) from 6D information, also present the escape speed curve from four Galactic potential models (Xue et al. 2008; Kenyon et al. 2014; McMillan 2017; Williams et al. 2017), the difference of curves illustrates the some uncertainties between these models. In the appendix, Table 2 provides Gaia identifiers, position, parallaxes, proper motions, distances and the Galaxy's velocity of HVSS with the probability of unbound $P_{\text{ub}} > 0.99$ from Gaia DR2 5D information and Table 3 provides the same parameters (the last column is the the probability of unbound) with $P_{\text{ub}} > 0.5$ from Gaia DR2 6D information. In the first column, the superscript 'B', 'H', 'M', and 'S' indicates that a source is also listed in Bromley et al. (2018), Hattori et al. (2018), Marchetti et al. (2018), and Scholz (2018), respectively.

Bromley et al. (2018) investigate the probability of stars not being bound using Gaia DR2 data. We find that 5 6D-unbound sources are also listed in their research. These stars have very high P_{ub} , and the little difference of P_{ub} may be due to the potential model. Hattori et al. (2018) trace the orbits of stars with extremely large velocities back in time and discuss the origin of these unbound stars. A 'HRS' and a 'OUT' candidates are also listed in their research, but the origins are undetermined in their study. Marchetti et al. (2018) search for unbound stars with Gaia DR2, and discuss their origin. We find that a 'OUT' and 3 'HRS' candidates are also listed in their research, and the conclusion about the origin of stars is consistent with theirs. Scholz (2018) study stars with high Galactic rest frame tangential velocities, and we find that 5 5D-unbound sources are also listed in their research.

3. SPATIAL DISTRIBUTION OF HVSS

The spatial distributions of HVSS on the sky can place useful constraints on their origin. For example, the massive black

hole (MBH) in the Galactic center can eject HVSSs in all directions. Using a few late B-type unbound HVSSs, Brown et al.

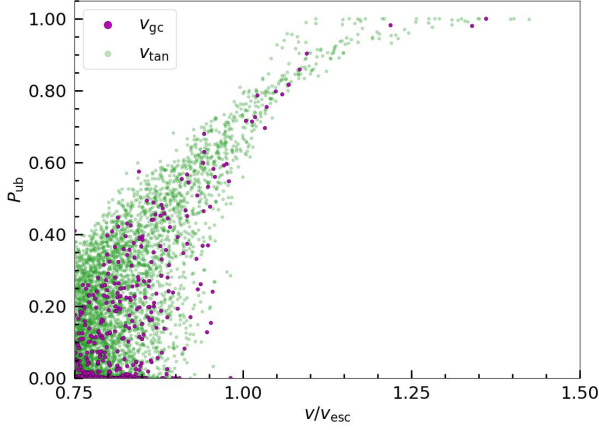


FIG. 1.— The probability of unbound P_{ub} as a function of velocity in the Galactic rest-frame V_{gc} for stars with $V > 0.75V_{esc}$. The green dots represent tangential velocities from proper motion of 5D information and the purple dots represent the total velocities from radial velocity and proper motion of 6D information. Only stars with $V > 0.75V_{esc}$ are considered in this study.

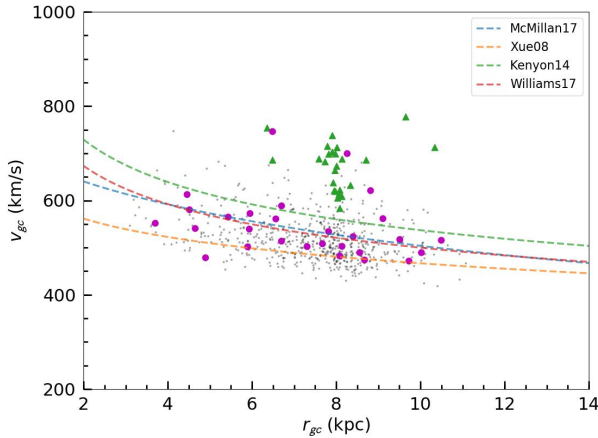


FIG. 2.— Total velocity in the Galactic rest-frame v_{gc} as a function of Galactocentric distance r_{gc} for stars with $P_{ub} > 0.5$ (black dots) and with $P_{ub} > 0.99$ (green triangles) from 5D information and stars with $P_{ub} > 0.5$ (purple circles) from 6D information. Four different colors dashed curves are median escape speeds from different Galaxy potential models (Xue et al. 2008; Kenyon et al. 2014; McMillan 2017; Williams et al. 2017).

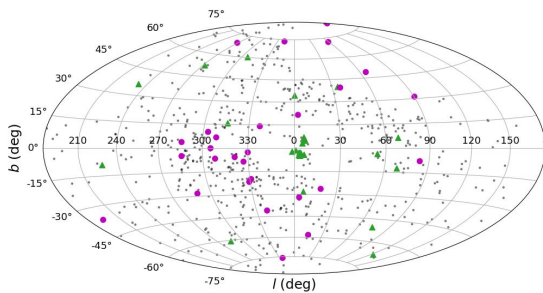


FIG. 3.— The spatial distribution of stars in the Galactic coordinate with $P_{ub} > 0.5$ (black dots) and with $P_{ub} > 0.99$ (green triangles) from 5D information and with $P_{ub} > 0.5$ (purple circles) from 6D information.

(2009, 2012, 2014) demonstrated that unbound HVSSs have a significantly anisotropic on the sky, while lower velocity bound HVSSs have a more isotropic distribution. We begin to study the trend by adopting 56 nearby late-type HVSSs. Figure 3 plots the angular position of these HVSSs in the Galactic coordinate. HVSSs with $P_{ub} > 0.99$ (which we call 5D-unbound) are marked with green triangles and possible unbound HVSSs with $P_{ub} > 0.5$ (which we call 5D-possible-unb) are marked with black dots from 5D information and possible unbound HVSSs with $P_{ub} > 0.5$ (which we call 6D-unbound) from full 6D information are marked with purple circles. Figure 4 also shows the spatial distribution of stars in Cartesian Galactocentric coordinate system. We can notice that most of unbound HVSSs in our sample are presently locate at nearby the Galactic plane, particularly a few unbound HVSSs are significantly clustered together around the solar neighborhood.

Green et al. (2019) present a three-dimensional map of dust reddening, based on Gaia parallaxes and stellar photometry from Pan-STARRS 1 and 2MASS. We use the ‘bayestar2019’ version of the 3D dust map and apply the median reddening for each stars. The optical extinction can be derive from the color excess:

$$A_V = 3.1 E(B - V). \quad (5)$$

Then we convert it to the Gaia passbands (Bromley et al. 2018):

$$A_G \approx 0.848A_V. \quad (6)$$

Figure 5 shows the HR diagram for 5D-unbound (green triangles) and 6D-unbound (purple circles) HVSSs and all stars with $V_{gc} > 0.75V_{esc}$ (black dots). The x-axis represents the color index in the Gaia Blue Pass (BP) and Red Pass (RP) bands BP-RP, and the y-axis gives the absolute magnitude in the Gaia G band. We can see that some unbound HVSSs are giants and also a few dwarfs, and these HVSSs are late type stars.

In order to test if the spatial distributions of unbound HVSSs and lower unbound probability HVSSs differ significantly, we use Kolmogorov-Smirnov (K-S) tests (See also Brown et al. 2009, 2012) which has the advantage of making no assumption about the distribution of data. Figure 6 gives the cumulative distribution of the Galactic longitude l and b for 6D-unbound (purple line) and 5D-unbound (green line) HVSSs. Firstly, K-S test derive isotropic distribution in longitudes and latitudes of 28 6D-unbound (purple line). Then for 28 5D-unbound, K-S tests give the likelihoods of 1.98×10^{-6} for the unbound HVSSs in same longitude distributions as the lower unbound probability. We derive the significance of 3.9σ by taking 10,000 random draws of 5D-possible-unb HVSSs. The likelihoods is 0.017 and significance is 2.37σ for the Galactic latitude. Thus the distribution of unbound HVSSs appears anisotropic in the Galactic longitude at more than 3σ level, which verifies the results provided in Brown et al. (2009, 2012). de la Fuente Marcos (2019) use the subsample with the lowest uncertainties to show the spatial distribution of hypervelocity star candidates is anisotropic, but they consider the origin of such an anisotropy is probably the result of observational biases and selection effects.

Similarly, we also consider the anisotropy in the distribution of angular separations of unbound HVSSs compared to the lower unbound probability HVSSs. Figure 7 plots the cumulative distribution of the angular separations, θ , of 6D-unbound (purple line) and 5D-unbound (green line) HVSSs. Calculating the angular separations for all unique pairs of stars, a K-

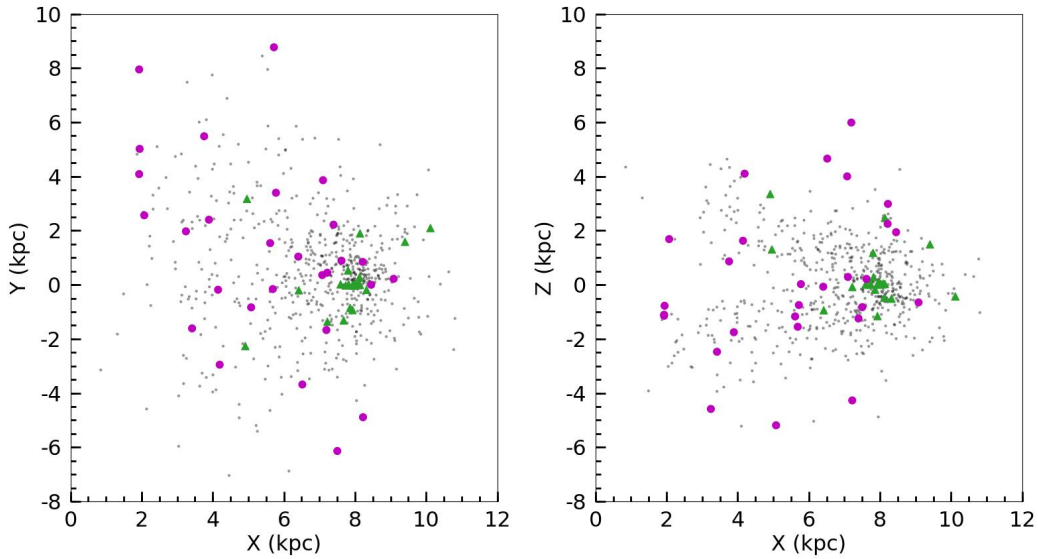


FIG. 4.— The spatial distribution of stars in Cartesian Galactocentric coordinate system with $P_{\text{ub}} > 0.5$ (black dots) and with $P_{\text{ub}} > 0.99$ (green triangles) from 5D information and with $P_{\text{ub}} > 0.5$ (purple circles) from 6D information.

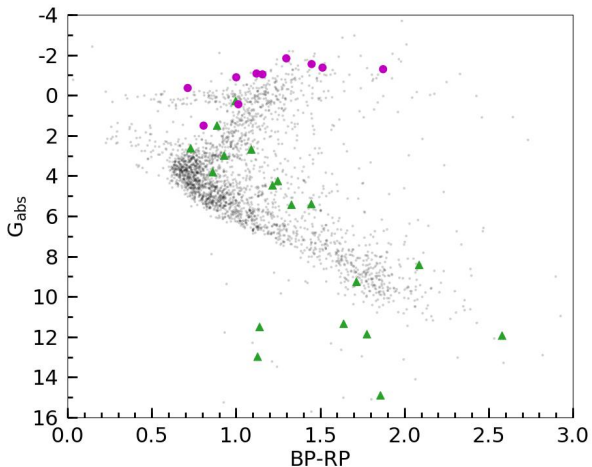


FIG. 5.— The HR diagram for the unbound HVSSs with $P_{\text{ub}} > 0.99$ (green triangles) from 5D information and HVSSs with $P_{\text{ub}} > 0.5$ (purple circles) from 6D information and all stars with $V_{\text{gc}} > 0.75V_{\text{esc}}$ (black dots).

S test derives that lower unbound probability HVSSs have a more isotropic distribution of angular separations. But for 5D-unbound HVSSs, the K-S test gives a 1.34×10^{-16} likelihood that are drawn from the same distribution of angular separations as the lower unbound probability HVSSs and the significance is 3.3σ . So the angular separation distribution of unbound HVSSs also shows anisotropic. Therefore, the new HVSSs discoveries that also include a few candidates in the southern sky of Gaia DR2 prove the previous claim of unbound HVS spatial anisotropy and lower velocity stars spatial isotropy distribution (See Brown et al. 2009, 2012).

4. POSSIBLE ORIGIN OF THE SPATIAL ANISOTROPY

We can derive the origin of stars from the position of these star crossing the disk (Marchetti et al. 2018). The minimum value of the distance from the Galactic center to the crossing point is called R_{min} . For each 6D-unbound HVS, we use the

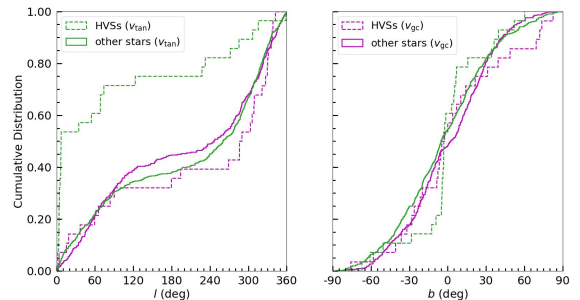


FIG. 6.— Cumulative distribution of the Galactic longitude l and b for unbound HVSSs and lower unbound probabilities HVSSs. The purple dashed line represent 28 lower unbound probabilities HVSSs with $P_{\text{ub}} > 0.5$ and purple solid line represents other stars with $P_{\text{ub}} < 0.5$ and $V > 0.75V_{\text{esc}}$ from 6D information. The green dashed line represent 28 unbound HVSSs with $P_{\text{ub}} > 0.99$ and the green solid line is other 619 lower velocity HVSSs with $P_{\text{ub}} > 0.5$ from 5D information.

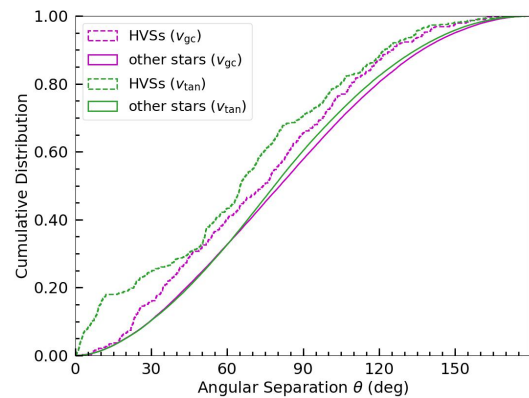


FIG. 7.— Cumulative distribution of angular separations for unbound HVSSs from 5D information and lower unbound probabilities HVSSs from 6D information. The colors show the same as Figure 6.

MCMC realizations discussed above and integrate each orbit back in a total time of 5 Gyr. Then we define the probability that a star is derived from the Galactic center P_{gc} ($R_{min} < 1$ kpc) and from the Galaxy P_{MW} ($R_{min} < 25$ kpc, Xu et al. (2015)). The classified criteria of stars' origin are shown in Table 1. We find 3 hypervelocity stars (HS) that could originate in the Galactic center, 12 stars with extragalactic origin (OUT) and 13 hyper-runaway star (HRS) candidates (see also Du et al. 2018b).

TABLE 1 The probability of stars are used as the classified criteria

Class	P_{gc}	P_{MW}
HS candidates	> 0.16	-
OUT candidates	< 0.16	< 0.5
HRS candidates	< 0.16	> 0.5

A number of models have been proposed to explain the spatial anisotropy of HVSSs. Each model predicts different spatial distributions of HVSSs. One model is the origin from the interaction between a single star and a hypothetical binary MBH (Yu & Tremaine 2003; Sesana et al. 2006, 2007; Merritt 2006), the interaction between a globular cluster with a binary MBH in the GC (e.g., Capuzzo & Fragione 2015; Fragione & Capuzzo-Dolcetta 2016). The binary black hole preferentially ejects HVSSs from its orbital plane. Thus the expected signature of a binary black hole in-spiral event is a ring or shell of HVSSs around the sky (Gualandris et al. 2005; Levin 2006; Sesana et al. 2006, 2007), the resulting HVS distribution in this scenario may be isotropic. Lu et al. (2010) and Zhang et al. (2010, 2013) propose that the HVSSs anisotropy reflects the anisotropic distribution of stars in the Galactic center. If HVSSs are ejected by the central MBH, then the direction of ejection corresponds to the direction that their progenitors encounter the MBH. In addition, the Galactic center contains many structures such as the molecular gas circumnuclear disk and ionized northern arm and stellar disk. Dynamical interactions between stellar disk and gas disk may scatter stars toward MBH to formate the S-stars and the HVSSs (Perets et al. 2009; Perets & Šubr 2012). Thus the Galactic center may provide a source for the observed anisotropy of HVSSs from the GC.

But as shown in Du et al. (2018b), most of nearby late-type HVSSs could not origin from the Galactic center and many nearby HVSSs are runaway stars candidates which originate from the disk of the Galaxy. Some previous surveys near the Galactic disk identify unbound stars ejected from the disk (Heber et al. 2008; Przybilla et al. 2008; Tillich et al. 2009; Irrgang et al. 2010; Li et al. 2018) as runaway stars mechanisms (Portegies 2000; Gvaramadze et al. 2009; Bromley et al. 2009; Wang et al. 2013; Wang 2018). The ejected star was boosted by Galactic rotation to overcome the Galactic escape velocity. Bromley et al. (2009) compared the simulated runaways with observations and derived that simulated runaways with radial velocities exceeding 400 km s^{-1} are located at low latitude $|b| < 45$ and in the direction of Galactic rotation; observed $> 400 \text{ km s}^{-1}$ runaways at $R = 50$ kpc are distributed uniformly across high latitude over all Galactic longitudes (Brown et al. 2012). Thus, the simulated distribution of runaway longitudes and latitude is inconsistent with the observed distribution of HVSSs.

An LMC origin of some HVSSs (e.g. HE 0437-5439) was pointed out because of their proximity to the LMC on the sky. Edelman et al. (2005) suggested HE 0437-5439 was ejected from the Large Magellanic Cloud (LMC) because that it was too young to have traveled from the GC to its present position. Later, the LMC origin of many more HVSSs was hypothesized by Boubert & Evans (2016) and Boubert et al. (2017), which was motivated by the clustering of many HVSSs in the constellation Leo (see reviews Brown et al. 2015). Abadi et al. (2009) propose that the HVSSs anisotropy also comes from the stellar ejecta of a tidally disrupted dwarf galaxy which is anisotropic in the sky (See also Teyssier et al. 2009; Piffl et al. 2011). But Brown et al. (2009, 2012) consider tidal debris an unlikely explanation for the observed HVSSs because no other unbound tidal debris is observed in the same region of sky and no dwarf galaxy in the Local Group has high velocity in the past. But Fritz et al. (2018) and Hammer et al. (2018) derive the new results that some dwarf galaxies have firstly high velocity using Gaia DR2 proper motions.

Finally, Brown et al. (2012, 2014) propose that the HVS anisotropy could reflect the anisotropic Galactic gravitational potential. Because many HVSSs are marginally unbound, a non-spherical potential can naturally explain why HVSSs are found in preferred directions on the sky: Stars ejected along the major axis of the potential are decelerated less than those ejected along the minor axis. An initially isotropic distribution of marginally unbound HVSSs can thus appear anisotropic in the halo. The predicted distribution of HVSSs depends on the axis ratio and the rotation direction of the potential. Up to now, there are no good constraints on the shape and orientation of the Galactic potential, it is difficult to judge if HVSSs anisotropy origin from Galactic gravitational potential.

5. CONCLUSIONS AND SUMMARY

Based on Gaia DR2 5D information of stars with parallax and proper motion but no radial velocity, we define our HVSSs sample as those stars with $V_{tan} > 0.75V_{esc}$ and identify 28 nearby (less than 6 kpc) late-type HVSSs with nearly 99% unbound possibility. At the same time, we also define the HVSSs candidate with $V_{gc} > 0.75V_{esc}$ from Gaia DR2 6D information from parallax, proper motion and radial velocity, 28 stars have probabilities greater than 50% of being unbound from the Galaxy, but only three has a nearly 99% probabilities of being unbound. It also indicates for these distance (~ 10 kpc) that is closer to the sun and to the Galactic center, tangential motion is more significant for nearby HVSSs. As predicted by Kenyon et al. (2018), radial velocities select HVSSs at large distances beyond ~ 10 kpc, tangential velocities selects the nearby fast-moving stars. On our HVSSs sample, there is 12 sources reported by other works and they are also marked in the Table.

We use Kolmogorov-Smirnov (K-S) tests to determine the spatial distributions of unbound HVSSs and lower unbound probability HVSSs. Lower unbound probability HVSSs are more isotropic and unbound HVSSs are spatially anisotropic at more than 3σ level, particularly in the Galactic longitude and angular separation, which strengthen the results provided in Brown et al. (2009, 2012) by using more HVSSs distributed in the whole sky. In addition, most of the confirmed HVSSs in previous studies are distant early-type stars due to the selections bias of target surveys, which is different from the nearby late-type HVSSs in this study, so the new identified HVSSs have different spatial distributions from previously identified sources. The observed spatial anisotropy of HVSSs could be

linked to their origin. We simply discuss the possible origin of HVSSs. In the near future, we also look forward to the accurate radial velocity observation for our HVSSs sample and it can provide the trajectory calculations to give a direct test of HVSSs origin. We also expect the future surveys will provide a rich source of more HVSSs discoveries.

ACKNOWLEDGEMENTS

We thank especially the referee for insightful comments and suggestions, which have improved the paper significantly. This work was supported by joint funding for Astronomy by the National Natural Science Foundation of China and the Chinese Academy of Science, under Grants U1231113. This work was also supported by the Special funds of cooperation between the Institute and the University of the Chinese Academy of Sciences, and China Scholarship

Council (CSC). In addition, this work was supported by the National Natural Foundation of China (NSFC No.11625313 and No.11573035). HJN acknowledges funding from NSF grant AST 16-15688. Funding for SDSS-III has been provided by the Alfred P. Sloan Foundation, the Participating Institutions, the National Science Foundation, and the U.S. Department of Energy Office of Science. This project was developed in part at the 2016 NYC Gaia Sprint, hosted by the Center for Computational Astrophysics at the Simons Foundation in New York City. This work has made use of data from the European Space Agency (ESA) mission Gaia (<http://www.cosmos.esa.int/gaia>), processed by the Gaia Data Processing and Analysis Consortium (DPAC, <http://www.cosmos.esa.int/web/gaia/dpac/consortium>). Funding for DPAC has been provided by national institutions, in particular the institutions participating in the Gaia Multilateral Agreement.

REFERENCES

- Abadi, M. G., Navarro, J.F., Steinmetz, M., 2009, *ApJL*, 691, L63
 Astraatmadja, T. L., & Bailer-Jones, C. A. L. 2016, *ApJ*, 833, 119
 Bailer-Jones C. A. L., 2015, *PASP*, 127, 994
 Bailer-Jones, C. A. L., Rybizki J., Fousneau, M., Mantelet, G., et al. 2018, *AJ*, 156, 58
 Bland-Hawthorn, J., Gerhard, O., 2016, *ARA&A*, 54, 529
 Bond, N. A., Ivezić, Ž, Sesar, B., et al. 2010, *ApJ* 716, 1
 Bromley, B. C., Kenyon, S. J., Brown, W. R., Geller M. J. 2009, *ApJ*, 706, 925
 Bromley, B. C., Kenyon, S. J., Brown, W. R., Geller, M. J. 2018, 868, 25
 Brown, W. R., Geller, M. J., Kenyon, S. J., & Kurtz, M. J. 2005, *ApJL*, 622, L33
 Brown, W. R., Geller, M. J., Kenyon, S. J., & Kurtz, M. J. 2006, *ApJ*, 647,303
 Brown, W. R., Geller, M. J., & Kenyon, S. J. 2009, *ApJ*, 690, 1639
 Brown, W. R., Geller, M. J., & Kenyon, S. J. 2012, *ApJ*, 751, 55
 Brown, W. R., Geller, M. J., & Kenyon, S. J. 2014, *ApJ*, 787, 89
 Brown, W. R. 2015, *ARA&A*, 53, 15
 Brown, W. R., Lattanzi, M. G., Kenyon, S. J., Geller, M. J., 2018, *ApJ*, 866, 39
 Boubert, D., & Evans, N. W. 2016, *ApJ*, 825, L6
 Boubert, D., Erkal, D., Evans, N. W., & Izzard, R. G. 2017, *MNRAS*, 469, 2151
 Boubert, D., Guillochon, J., Hawkins, K., Ginsburg, I., Evans, N. W., et al. 2018, *MNRAS*, 479, 2789
 Butkevich, A. G., Klioner, S. A., Lindegren, L., Hobbs, D., et al. 2017, *A&A*, 603, A45
 Capuzzo-Dolcetta, R., Fragione, G., 2015, *MNRAS*, 454, 2677
 de la Fuente Marcos, R., & de la Fuente Marcos, C. 2019, *arXiv:1906.05227*
 Du, C. H., Li, H. F., Liu S., Donlon, T., Newberg, H. J. 2018, *ApJ*, 863, 87
 Du, C. H., Li, H. F., Newberg, H.J., Chen, Y. Q., Shi, J. R. 2018, *ApJL*, 869, 31
 Edelmann, H., Napiwotzki, R., Heber, U., Christlieb, N., & Reimers, D. 2005, *ApJ*, 634, L181
 Foreman-Mackey, D., Hogg, D. W., Lang, D., Goodman, J., 2013, *PASP*, 125, 306
 Fragione, G., Capuzzo-Dolcetta, R. 2016, *MNRAS*, 458, 2596
 Fritz, T. K., Battaglia, G., Pawlowski, M. S., Kallivayalil, N., Marel, v.d., et al. 2018, *A&A*, 619, A103
 Gaia Collaboration, Brown, A. G. A., Vallenari, A., et al. 2016, *A&A*, 595, A2
 Gaia Collaboration (Brown, A.G.A.), et al. 2018a, *A&A*, 616, A1
 Gaia Collaboration (Katz, D.), et al. 2018b, *A&A*, 616, A11
 Geier, S., Fürst, F., Ziegerer, E., et al. 2015, *Science*, 347, 1126
 Gnedin, O. Y., Gould, A., Miralda-Escudé, J., & Zentner, A. R. 2005, *ApJ*, 634, 344
 Goodman, J., Weare, J., 2010, *CAMCS.*, 5, 65
 Green, G. M., Schlafly, E. F., Zucker, C., Speagle, J. S., Finkbeiner, D. P., *arXiv:1905.02734*
 Gualandris, A., Portegies Zwart, S. P., & Sipior, M. S., 2005, *MNRAS*, 363, 223
 Gvaramadze, V. V., Gualandris, A., Portegies, Zwart S., 2009, *MNRAS*, 396, 570
 Hammer, F., Yang, Y. B., Arenou, F., Babusiaux, C., Wang, J. L., et al. 2018, *ApJ*, 860, 76
 Hattori, K., Valluri, M., Bell, E. F., & Roederer, I. U., 2018, *ApJ*, 866, 121
 Hawkins, K., Kordopatis, G., Gilmore, G., Masseron, T., et al. 2015, *MNRAS*, 447, 2046
 Heber, U., Edelmann, H., Napiwotzki, R., Altmann, M., & Scholz, R.-D. 2008, *A&A*, 483, L21
 Hills, J. G., 1988, *Nature*, 331, 687
 Hirsch, H. A., Heber, U., O'Toole, S. J., & Bresolin, F., 2005, *A&A*, 444, L61
 Huang, Y., Liu, X. W., Zhang, H. W., et al. 2017, *ApJ*, 847, 9
 Irrgang, A., Przybilla, N., Heber, U., Fernanda Nieva, M., & Schuh, S. 2010, *ApJ*, 711, 138
 Irrgang, A., Kreuzer, S., Heber, U., 2018, *A&A*, 620, 481
 Johnson, D. R. H., & Soderblom D. R., 1987, *AJ*, 93, 864
 Jurić M., Ivezić, Ž., Brooks, A., et al. 2008, *ApJ*, 673, 864
 Kenyon, S. J., Bromley, B. C., Brown, W. R., & Geller, M. J. 2014, *ApJ*, 793, 122
 Kenyon, S. J., Bromley, B. C., Brown, W. R., & Geller, M. J. 2018, *ApJ*, 864, 130
 Kollmeier, J. A., Gould, A., Knapp, G., et al. 2009, *ApJ*, 697, 1543
 Kollmeier, J. A., Gould, A., Rockosi, C., et al. 2010, *ApJ*, 723, 812
 Levin, Y., 2006, *ApJ*, 653, 1203
 Li, Y. B., Luo, A. L., Zhao, G., et al. 2012, *ApJL*, 744, L24
 Li, Y. B., Luo, A. L., Zhao, G., et al. 2018, *AJ*, 156, 87
 Lindegren, L., Hernández, J., Bombrun, A., et al. 2018, *AJ*, 616, A2
 Luri, X., Brown, A. G. A., Sarro, L. M., et al. 2018, *A&A*, 616, A9
 Lu, Y., Zhang, F., & Yu, Q., 2010, *ApJ*, 709, 1356
 McMillan, P. J. 2017, *MNRAS*, 465, 76
 Marchetti, T., Rossi, E. M., & Brown, A. G. A. 2018, *MNRAS*, *arXiv:1804.10607v1*
 Merritt, D. 2006, *ApJ*, 648, 976
 Palladino, L. E., Schlesinger, K. J., Holley-Bockelmann, K., et al. 2014, *ApJ*, 780, 7
 Perets, H. B., Gualandris, A., Merritt, D., & Alexander, T. 2009, *ApJ*, 702, 884
 Perets, H. B., & Šubr, L., 2012, *ApJ*, 751, 133
 Piffl, T., Williams, M., & Steinmetz, M., 2011, *A&A*, 535, A70
 Piffl, T. et al. 2014, *A&A*, 562, A91
 Portegies, Zwart S. F., 2000, *ApJ*, 544, 437
 Przybilla, N., Nieva, M. F., Heber, U., & Butler, K. 2008, *ApJ*, 684, L103
 Purcell, C. W., Bullock, J. S., & Kazantzidis S. 2010, *MNRAS*, 404, 1711
 Raddi, R., Hollands, M. A., Koester, D., et al. 2018, *ApJ*, 858, 3
 Scholz, R.-D. 2018, *RNASS*, 2, 211
 Sesana, A., Haardt, F., & Madau, P. 2006, *ApJ*, 651, 392
 Sesana, A., Haardt, F., & Madau, P. 2007, *MNRAS*, 379, L45
 Sesana, A., Haardt, F., & Madau, P. 2008, *ApJ*, 686, 432
 Shen, K. J., Boubert, D., Gänsicke, B. T., et al. 2018, *ApJ*, 865, 15
 Smith M. C. et al. 2007, *MNRAS*, 379, 755
 Tauris, T.M., 2015, *MNRAS Lett.*, 448, L6
 Teysier, M., Johnston, K. V., & Shara, M. M., 2009, *ApJL*, 707, L22
 Tian, H. J., Liu, C., Carlin, J. L., et al. 2015, *ApJ*, 809, 145
 Tillich, A., Przybilla, N., Scholz, R., & Heber, U. 2009, *A&A*, 507, L37

- Xue, X. X., Rix, H. W., Zhao, G., et al. 2008, *ApJ*, 684, 1143
Vennes, S., Nemeth, P., Kawka, A., et al. 2017, *Science*, 357, 680
Vickers, J. J., Smith, M. C., & Grebel, E. K. 2015, *AJ*, 150, 77
Wang, B., & Han, Z., 2009, *A&A*, 508, L27
Wang, B., Justham, S., & Han, Z., 2013, *A&A*, 559, A94
Wang, B., 2018, *RAA*, Vol.18, No.5, 49
Williams, A. A., Belokurov, V., Casey, A. R., Evans, N. W., 2017, *MNRAS*, 468, 2359
Xu, Y., Newberg, H. J., Carlin, J. L., et al. 2015, *ApJ*, 801, 105
Yu, Q., & Tremaine, S., 2003, *ApJ*, 599, 1129
Zhang, F., Lu, Y., & Yu, Q. 2010, *ApJ*, 722, 1744
Zhang, F., Lu, Y., & Yu, Q. 2013, *ApJ*, 768, 153
Zhang, Y. Q., Smith, M. C., Carlin, J. L., 2016, *ApJ*, 832, 10
Zheng, Z., Carlin, J. L., Beers, T. C., et al. 2014, *ApJL*, 785, 23
Zhong, J., Chen, L., Liu, C., et al. 2014, *ApJL*, 789, L2
Ziegerer, E., Volkert, M., Heber, U., et al. 2015, *A&A*, 576, L14
Ziegerer, E., Heber, U., Geier, S., et al. 2017, *A&A*, 601, A58

APPENDIX

TABLE 2 HVS identified from tangential velocity selection of Gaia DR2 5D information

source-id	(<i>l</i> , <i>b</i>) (deg)	ϖ (mas)	μ_{α^*} (mas yr ⁻¹)	μ_{δ} (mas yr ⁻¹)	<i>d</i> (kpc)	<i>r_{gc}</i> (kpc)	<i>v_{gc}</i> (km s ⁻¹)
6698855754225352192 ^S	(6.57, -28.38)	0.494 ± 0.047	-38.97 ± 0.07	-86.57 ± 0.05	2.11 ^{+0.24} _{-0.19}	6.44 ^{+0.15} _{-0.18}	717 ⁺¹⁰⁶ ₋₈₅
3593446274383096448 ^S	(271.8, 52.16)	0.299 ± 0.04	-36.35 ± 0.06	-47.94 ± 0.04	3.26 ^{+0.48} _{-0.35}	8.77 ^{+0.18} _{-0.12}	734 ⁺¹³⁶ ₋₁₀₀
4119670443586493184	(6.86, 4.77)	4.211 ± 0.585	249.85 ± 1.79	216.73 ± 1.51	0.28 ^{+0.06} _{-0.04}	7.93 ^{+0.04} _{-0.06}	670 ⁺⁹⁹ ₋₆₈
1842456376310935552	(68.53, -12.51)	1.092 ± 0.175	-131.96 ± 0.29	-108.69 ± 0.31	1.09 ^{+0.27} _{-0.19}	7.87 ^{+0.05} _{-0.06}	824 ⁺²²⁰ ₋₁₅₄
4396109004117478656	(0.46, 34.34)	2.215 ± 0.225	-359.69 ± 0.46	-228.42 ± 0.29	0.47 ^{+0.05} _{-0.05}	7.81 ^{+0.04} _{-0.04}	728 ⁺⁹² ₋₉₀
4912074832815572224	(285.44, -60.68)	1.758 ± 0.254	-101.33 ± 0.39	-246.8 ± 0.36	0.63 ^{+0.12} _{-0.08}	8.14 ^{+0.01} _{-0.01}	756 ⁺¹⁵¹ ₋₁₀₁
4119759641435130624	(7.04, 5.46)	4.807 ± 0.676	285.92 ± 1.87	244.62 ± 1.66	0.24 ^{+0.06} _{-0.04}	7.96 ^{+0.03} _{-0.05}	663 ⁺⁹⁸ ₋₆₂
4065092915465740160	(6.43, -4.25)	6.248 ± 0.638	335.49 ± 1.49	342.42 ± 1.44	0.17 ^{+0.02} _{-0.02}	8.03 ^{+0.02} _{-0.02}	621 ⁺⁵⁵ ₋₄₀
2946665465655257472 ^B	(227.47, -9.16)	0.345 ± 0.057	54.42 ± 0.1	11.06 ± 0.13	3.26 ^{+0.76} _{-0.54}	10.65 ^{+0.63} _{-0.43}	810 ⁺¹⁹⁸ ₋₁₃₉
4467323685050696960	(34.57, 39.8)	0.177 ± 0.028	-2.8 ± 0.03	-36.58 ± 0.03	5.58 ^{+0.9} _{-0.67}	6.39 ^{+0.11} _{-0.02}	819 ⁺¹⁵⁵ ₋₁₁₅
3841458366321558656 ^S	(232.7, 36.34)	0.363 ± 0.063	7.29 ± 0.11	-81.39 ± 0.11	2.63 ^{+0.45} _{-0.32}	9.77 ^{+0.31} _{-0.21}	840 ⁺¹⁷⁵ ₋₁₂₂
2655054950237153664	(73.95, -50.53)	0.65 ± 0.03	84.99 ± 0.05	-65.81 ± 0.05	1.55 ^{+0.07} _{-0.07}	8.07 ^{+0.0} _{-0.0}	621 ⁺³⁷ ₋₃₃
4062943374550066560	(3.44, -3.05)	9.043 ± 0.614	494.36 ± 1.08	439.52 ± 0.87	0.11 ^{+0.01} _{-0.01}	8.09 ^{+0.01} _{-0.01}	589 ⁺²⁸ ₋₂₃
4121504428896960640	(6.38, 6.9)	9.146 ± 0.932	580.45 ± 2.88	453.91 ± 2.37	0.12 ^{+0.02} _{-0.01}	8.08 ^{+0.01} _{-0.01}	648 ⁺⁵⁷ ₋₄₂
2047267531138612864	(68.53, 6.39)	0.714 ± 0.081	-0.26 ± 0.11	96.36 ± 0.16	1.5 ^{+0.2} _{-0.18}	7.78 ^{+0.04} _{-0.04}	748 ⁺⁵⁷ ₋₈₀
4050754184394584192	(3.03, -4.6)	3.811 ± 0.39	224.82 ± 0.84	223.44 ± 0.79	0.28 ^{+0.03} _{-0.03}	7.92 ^{+0.03} _{-0.03}	656 ⁺⁵⁰ ₋₄₂
2525871954701579904	(123.07, -67.05)	1.709 ± 0.062	257.34 ± 0.14	-162.88 ± 0.1	0.59 ^{+0.02} _{-0.02}	8.34 ^{+0.01} _{-0.01}	636 ⁺³⁰ ₋₂₇
3685380427311132160	(306.79, 60.27)	0.752 ± 0.063	26.92 ± 0.14	-134.33 ± 0.07	1.36 ^{+0.12} _{-0.1}	7.91 ^{+0.01} _{-0.01}	761 ⁺⁷³ ₋₆₅
4050705707044344832	(3.87, -4.94)	4.499 ± 0.46	283.27 ± 0.96	281.43 ± 0.9	0.24 ^{+0.03} _{-0.02}	7.96 ^{+0.02} _{-0.03}	685 ⁺⁵⁰ ₋₄₅
4052470217026086144	(4.19, -4.39)	5.779 ± 0.76	413.64 ± 1.27	385.05 ± 1.13	0.2 ^{+0.04} _{-0.04}	8.0 ^{+0.03} _{-0.04}	772 ⁺¹⁰¹ ₋₇₄
4055741088022263680	(358.71, -2.32)	1.722 ± 0.264	119.84 ± 1.04	102.69 ± 0.87	0.69 ^{+0.17} _{-0.11}	7.51 ^{+0.11} _{-0.17}	751 ⁺¹²⁵ ₋₈₄
4057367235624058240	(1.14, -1.46)	5.505 ± 0.667	373.14 ± 1.31	324.91 ± 1.04	0.2 ^{+0.04} _{-0.03}	8.0 ^{+0.03} _{-0.04}	711 ⁺⁸³ ₋₅₉
4062949009547937152	(3.59, -3.05)	2.21 ± 0.241	148.13 ± 0.91	140.71 ± 0.87	0.49 ^{+0.06} _{-0.03}	7.71 ^{+0.05} _{-0.05}	708 ⁺⁶³ ₋₅₄
4063041295654767488	(3.77, -3.23)	3.779 ± 0.401	498.53 ± 0.78	445.61 ± 0.69	0.29 ^{+0.03} _{-0.03}	7.91 ^{+0.03} _{-0.03}	1142 ⁺¹⁰⁹ ₋₁₀₁
4063270135632421888	(4.33, -3.13)	4.836 ± 0.665	325.47 ± 1.49	319.65 ± 1.27	0.24 ^{+0.06} _{-0.03}	7.96 ^{+0.03} _{-0.06}	751 ⁺¹²⁶ ₋₇₄
4068950625022563584	(5.38, 3.03)	16.07 ± 1.036	980.72 ± 2.86	799.44 ± 2.4	0.06 ^{+0.0} _{-0.0}	8.14 ^{+0.0} _{-0.0}	611 ⁺²⁵ ₋₂
1820931585123817728	(54.4, -3.67)	0.602 ± 0.076	-82.41 ± 0.09	-149.53 ± 0.09	1.8 ^{+0.51} _{-0.21}	7.3 ^{+0.0} _{-0.12}	1319 ⁺²⁵² ₋₁₇₃
6097052289696317952 ^S	(315.6, 15.74)	0.202 ± 0.033	-61.1 ± 0.05	-24.73 ± 0.05	5.1 ^{+0.85} _{-0.68}	6.0 ^{+0.11} _{-0.04}	1407 ⁺²⁶⁵ ₋₂₁₄

TABLE 3 HVS identified from total velocity selection of Gaia DR2 6D information

source-id	(<i>l</i> , <i>b</i>) (deg)	ϖ (mas)	μ_{α^*} (mas yr ⁻¹)	μ_{δ} (mas yr ⁻¹)	<i>rv</i> (km s ⁻¹)	<i>d</i> (kpc)	<i>r_{gc}</i> (kpc)	<i>v_{gc}</i> (km s ⁻¹)	<i>P_{ub}</i>
HS candidates									
6075020928535605632	(303.2, 10.18)	0.943 ± 0.107	-113.45 ± 0.11	3.83 ± 0.1	-55.9 ± 0.7	1.16 ^{+0.16} _{-0.24}	7.64 ^{+0.06} _{-0.07}	546 ⁺⁷⁷ ₋₇₀	0.58
6009917672524909312	(337.28, 14.04)	0.138 ± 0.023	-20.43 ± 0.05	-5.98 ± 0.03	-145.4 ± 1.2	7.52 ^{+1.53} _{-1.05}	3.76 ^{+0.36} _{-0.08}	612 ⁺¹⁴⁶ ₋₉₄	0.60
5830453567907178368	(326.91, -8.61)	0.126 ± 0.02	-12.56 ± 0.03	-16.59 ± 0.03	155.8 ± 1.1	8.36 ^{+1.49} _{-1.23}	4.85 ^{+0.66} _{-0.24}	619 ⁺¹⁴⁶ ₋₁₂₁	0.63
OUT candidates									
3905884598043829504	(268.95, 69.21)	0.406 ± 0.041	-35.88 ± 0.08	-52.22 ± 0.04	149.7 ± 1.2	2.49 ^{+0.28} _{-0.24}	8.59 ^{+0.09} _{-0.07}	522 ⁺⁸³ ₋₇₀	0.53
1436193190692538496	(90.29, 31.18)	0.161 ± 0.017	10.68 ± 0.04	-9.43 ± 0.04	-213.3 ± 0.8	5.93 ^{+0.61} _{-0.52}	10.15 ^{+0.37} _{-0.3}	503 ⁺⁴¹ ₋₃₅	0.55
6694147709857729920	(3.64, -32.07)	0.337 ± 0.048	-27.19 ± 0.07	-42.4 ± 0.05	-20.0 ± 0.4	3.26 ^{+0.61} _{-0.47}	5.7 ^{+0.31} _{-0.37}	570 ⁺¹⁴² ₋₁₀₈	0.55
6630656964968299264	(330.86, -19.83)	0.181 ± 0.035	-16.32 ± 0.03	-22.68 ± 0.04	148.3 ± 1.2	6.13 ^{+1.4} _{-1.05}	4.77 ^{+0.26} _{-0.2}	596 ⁺¹³⁷ ₋₁₃₄	0.57
6437621133019281408	(329.26, -21.67)	0.308 ± 0.029	-36.1 ± 0.03	-29.25 ± 0.04	252.9 ± 0.9	3.38 ^{+0.39} _{-0.31}	5.86 ^{+0.17} _{-0.2}	570 ⁺⁸³ ₋₆₄	0.60
5862473747352575104	(305.49, -0.04)	0.232 ± 0.045	-29.0 ± 0.05	-14.44 ± 0.06	80.3 ± 1.2	4.86 ^{+1.4} _{-0.88}	6.71 ^{+0.14} _{-0.03}	616 ⁺²¹² ₋₁₃₂	0.68
1478837543019912064 ^B	(59.01, 71.88)	0.134 ± 0.019	-17.61 ± 0.02	-16.57 ± 0.03	-245.9 ± 1.5	6.5 ^{+0.7} _{-0.67}	9.63 ^{+0.45} _{-0.35}	541 ⁺⁸⁶ ₋₇₂	0.70
5212110596595560192 ^H	(289.93, -28.26)	0.372 ± 0.018	9.98 ± 0.04	-34.43 ± 0.04	298.2 ± 0.5	2.71 ^{+0.13} _{-0.13}	7.82 ^{+0.01} _{-0.0}	540 ⁺²¹ ₋₂₁	0.71
5827258039189703808	(321.27, -5.71)	0.116 ± 0.02	-17.34 ± 0.03	-9.3 ± 0.03	51.1 ± 3.1	8.79 ^{+1.7} _{-1.24}	5.71 ^{+0.9} _{-0.41}	633 ⁺¹⁵⁷ ₋₁₁₅	0.72
4998248468230919936	(335.6, -75.95)	0.184 ± 0.036	16.68 ± 0.05	-30.9 ± 0.05	-139.8 ± 0.8	4.76 ^{+0.78} _{-0.61}	8.51 ^{+0.3} _{-0.19}	575 ⁺¹²⁴ ₋₉₆	0.73
6851832593704580224	(18.63, -26.36)	0.168 ± 0.03	-9.28 ± 0.05	-28.68 ± 0.03	-11.9 ± 2.4	6.37 ^{+1.35} _{-1.02}	4.42 ^{+0.28} _{-0.09}	685 ⁺¹⁹³ ₋₁₄₁	0.79
4326973843264734208 ^{M,B}	(2.6, 21.53)	0.228 ± 0.031	-20.55 ± 0.05	-33.97 ± 0.03	-220.4 ± 2.1	4.66 ^{+0.78} _{-0.58}	4.24 ^{+0.42} _{-0.5}	667 ⁺¹⁴¹ ₋₁₀₄	0.82
HRS candidates									
1964858172545721472	(83.52, -7.85)	0.148 ± 0.024	10.72 ± 0.04	10.55 ± 0.04	-151.0 ± 0.8	6.71 ^{+1.16} _{-0.92}	9.99 ^{+0.71} _{-0.5}	505 ⁺⁸¹ ₋₆₄	0.51
4015088951907615744	(179.69, 82.44)	0.482 ± 0.081	-62.98 ± 0.13	-6.65 ± 0.09	-54.7 ± 0.9	2.12 ^{+0.4} _{-0.31}	8.74 ^{+0.15} _{-0.11}	524 ⁺¹¹³ ₋₈₄	0.54
6601618897232424064	(14.97, -58.22)	0.134 ± 0.025	18.82 ± 0.04	-11.0 ± 0.04	-137.5 ± 2.2	6.47 ^{+1.02} _{-0.73}	7.41 ^{+0.37} _{-0.19}	534 ⁺⁹⁹ ₋₇₀	0.56

5353013183518841728	(285.9, 3.74)	0.239 ± 0.043	-9.21 ± 0.07	25.45 ± 0.06	275.1 ± 0.8	4.49 ^{+1.0} _{-0.68}	8.2 ^{+0.33} _{-0.16}	542 ⁺¹²⁹ ₋₈₇	0.57
3741464316420909952	(342.32, 73.51)	0.209 ± 0.036	-29.0 ± 0.08	4.3 ± 0.04	-55.4 ± 2.2	4.4 ^{+0.67} _{-0.55}	8.2 ^{+0.2} _{-0.13}	534 ⁺⁸⁶ ₋₆₉	0.59
5252990984378265984	(285.79, -4.86)	0.103 ± 0.018	-12.07 ± 0.03	5.35 ± 0.03	109.2 ± 1.4	9.93 ^{+2.13} _{-1.38}	11.03 ^{+1.38} _{-0.92}	564 ⁺¹³⁰ ₋₈₄	0.75
6456587609813249536 ^{M,B}	(338.3, -40.85)	0.128 ± 0.019	13.0 ± 0.03	-18.26 ± 0.03	-15.9 ± 2.8	7.48 ^{+1.2} _{-0.86}	6.06 ^{+0.44} _{-0.18}	616 ⁺¹²⁴ ₋₈₈	0.79
4563629049534297216	(36.39, 39.33)	0.131 ± 0.026	-23.11 ± 0.03	-4.04 ± 0.04	-41.7 ± 0.7	6.97 ^{+1.39} _{-0.91}	6.7 ^{+0.51} _{-0.2}	619 ⁺¹³⁰ ₋₉₇	0.80
6065230602133664000	(309.01, 6.77)	0.132 ± 0.021	-21.32 ± 0.04	-6.07 ± 0.04	104.0 ± 1.1	7.72 ^{+1.34} _{-0.98}	6.91 ^{+0.61} _{-0.31}	653 ⁺¹⁴⁰ ₋₁₀₃	0.86
3252546886080448384 ^H	(193.87, -36.61)	0.875 ± 0.064	16.45 ± 0.09	-136.1 ± 0.06	1.7 ± 4.9	1.16 ^{+0.09} _{-0.08}	9.13 ^{+0.07} _{-0.06}	574 ⁺⁵⁷ ₋₄₈	0.90
5847216962695435392	(308.26, -6.59)	0.087 ± 0.017	-15.91 ± 0.02	-7.34 ± 0.03	260.1 ± 18.2	11.55 ^{+2.19} _{-1.89}	9.17 ^{+1.66} _{-1.23}	812 ⁺¹⁸¹ ₋₁₅₇	0.98
1383279090527227264 ^{M,B}	(65.46, 48.85)	0.147 ± 0.016	-25.76 ± 0.03	-9.75 ± 0.04	-180.9 ± 2.4	6.44 ^{+0.66} _{-0.57}	8.95 ^{+0.33} _{-0.25}	658 ⁺⁸⁶ ₋₇₄	0.98
5932173855446728064 ^{M,B}	(329.94, -2.7)	0.483 ± 0.029	-2.68 ± 0.04	-4.99 ± 0.03	-614.3 ± 2.5	2.11 ^{+0.14} _{-0.13}	6.47 ^{+0.1} _{-0.11}	746 ⁺³ ₋₃	1.00